THE JOURNAL OF PHYSICAL CHEMISTRY B

ARTICLE

pubs.acs.org/JPCB

Phase Transformations Undergone by Triton X-100 Probed by Differential Scanning Calorimetry and Dielectric Relaxation Spectroscopy

Esther G. Merino,[†] Carla Rodrigues,[†] M. Teresa Viciosa,[‡] Carlos Melo,[†] João Sotomayor,[†] Madalena Dionísio,*[,†] and Natália T. Correia[†,§]

[†]REQUIMTE/CQFB, Departamento de Química, Faculdade de Ciências e Tecnologia, Universidade Nova de Lisboa, 2829-516 Caparica, Portugal

[‡]CQFM — Centro de Química-Física Molecular and IN — Institute of Nanoscience and Nanotechnology, Instituto Superior Técnico, Universidade Técnica de Lisboa, Avenida Rovisco Pais, 1049-001 Lisboa, Portugal

[§]Unité Matériaux et Transformation (UMET), UMR CNRS 8207, UFR de Physique, BAT P5, Université Lille 1, 59655 Villeneuve d'Ascq, France

ABSTRACT: The phase transformations of the surfactant Triton X-100 were investigated by differential scanning calorimetry (DSC), polarized optical microscopy (POM), and dielectric relaxation spectroscopy (DRS). In particular, crystallization was induced at different cooling rates comprised between 13 and 0.5 K min^{-1}. Vitrification was detected by both DSC and DRS techniques with a glass transition temperature of ~212 K (measured on heating by DSC) allowing classifying Triton X-100 as a glass former. A fully amorphous material was obtained by cooling at a rate ≥10 K min^{-1}, while crystallization was observed for lower cooling rates. The temperature of the onset of melt-crystallization was found to be dependent on the cooling scan rate, being higher the lower was the scan rate. In subsequent heating scans, the material undergoes cold-crystallization except if cooled previously at a rate ≤1 K min^{-1}. None of the different thermal histories led to a 100% crystalline material because always the jump typical of the glass transformation in both heat flux (DSC) and real permittivity (DRS) is observed. It was also observed that the extent/morphology of the crystalline phase depends on the degree of undercooling, with higher spherulites developing for lower undercooling degree ($24\ K \le T_m - T_{cr} \le 44\ K$) in melt-crystallization and a grain-like morphology emerging for $T_m - T_{cr} \approx 57$ K either in melt- or cold-crystallization. The isothermal cold- and melt-crystallizations were monitored near above the calorimetric glass transition temperature by POM (221 K) and real-time DRS (T_{cr} = 219, 220, and 221 K) to evaluate the phase transformation from an amorphous to a semicrystalline material. By DRS, the α-relaxation associated with the dynamic glass transition was followed, with the observation that it depletes upon both type of crystallizations with no significant changes either in shape or in location. Kinetic parameters were obtained from the time evolution of the normalized permittivity according to a modified Avrami model taking in account the induction time. The reason the isothermal crystallization occurs to a great extent in the vicinity of the glass transition was rationalized as the simultaneous effect of (i) a high dynamic fragile behavior and (ii) the occurrence of catastrophic nucleation/crystal growth probably enabled by a preordering tendency of the surfactant molecules. This is compatible with the estimated low Avrami exponent ($1.12 \le n \le 1.6$), suggesting that relative short length scale motions govern the crystal growth in Triton X-100 coherent with the observation of a grainy crystallization by POM.

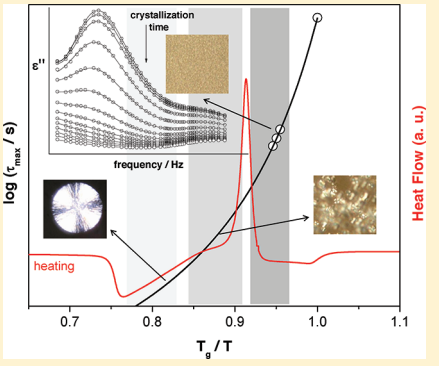

1. INTRODUCTION

The factors that govern the interconversion between amorphous and crystalline states and their stability are fundamental aspects of several areas of science and technology gaining special importance in pharmaceutical[1−3] and food[4] industries. Indeed, significant molecular mobility can persist in the glassy state enabling, for instance, the occurrence of phase transitions such as crystallization.[5−7] In this context, understanding key questions such as under what conditions an amorphous leads to crystal formation and the relation between temperature and crystallization pathways is most relevant in materials preservation.[1,2,8,9]

In this work, the water-soluble, liquid surfactant Triton-X 100, the molecular formula of which is $C_{14}H_{22}O(C_2H_4O)_n$ (with $n = 9-10$), was chosen to explore the different aspects concerning temperature-driven phase transformations because it is able to undergo both vitrification and crystallization. This nonionic detergent is widely used in industrial and pharmaceutical formulations and in biological applications such as solubilization of membrane proteins without losing their activity[10] and isolation of membrane rafts,[11] and it also forms transparent microemulsions capable of dissolving both water and oil in relatively large amounts.[12] Because of its high dielectric response and ability to crystallize

Received: March 25, 2011
Revised: August 5, 2011
Published: September 19, 2011

Scheme 1. Chemical Structure of Triton X-100; $n \approx 9-10$

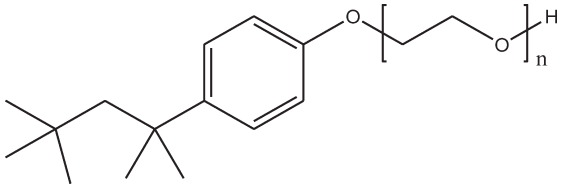

from both molten (melt-crystallization) and glassy (cold-crystallization) states, its isothermal crystallization was monitored in real time by dielectric relaxation spectroscopy (DRS) at temperatures nearly above the glass transition temperature ($T_g + 6 \leq T_{cr} \leq T_g + 8$) between 1 Hz and 1 MHz. The usual way that dielectric spectroscopy is used to follow isothermal crystallization is through the reduction of the dielectric strength of the process associated with the dynamical glass transition, α-relaxation, either in polymers like PET,[13,14] PLLA,[15−18] and polycarbonate/poly(ε-caprolactone) blends,[19] or low molecular weight materials such as isooctyloxycyanobiphenyl,[20] triphenyl phosphate,[21] sorbitol,[22] 2-propanol,[23] acetaminophen,[24] and another pharmaceutical drug,[25] terephthalic acid dipropyl ester,[26] and ethylene glycol dimethacrylate.[27] To our knowledge, studies involving DRS, DSC, and POM to probe molecular mobility and phase transformations (crystal−liquid, supercooled−crystal, supercooled liquid−glass) have not been reported for neat Triton X-100. Published results refer mainly to mixtures of Triton X-100 with water;[12] the dielectric behavior of the neat material is studied at room temperature only in a frequency range from 10^6 to 10^{10} Hz.[12]

The present work represents an additional contribution concerning crystallization behavior of low molecular weight glass formers. Moreover, the kinetics of isothermal crystallizations will be analyzed by the Avrami law[28] taking into account the induction time. Comparison with the kinetic behavior of another glass former, ethylene glycol dimethacrylate (EGDMA), will allow one to establish a correlation between the n Avrami exponent and morphology as observed by POM.

2. EXPERIMENTAL SECTION

2.1. Materials. Triton X-100, polyethylene glycol *tert*-octylphenyl ether, $C_{14}H_{22}O(C_2H_4O)_n$ (see Scheme 1), with an average number $n \approx 9-10$ of oxyethylene units per molecule (MW $\approx$ 625), was reagent grade purchased from Fluka (catalog number 93420; CAS number: 9002-93-1).

A Karl Fisher analysis showed water content of 0.28% (w/w). It was used without further purification.

Results for Triton X-100 were compared to another glass former, ethylene glycol dimethacrylate (EGDMA) supplied by Aldrich, catalog no. 33,568-1, MW = 198.22, 98% assay (used as received), which was measured by POM in the present work.

2.2. Differential Scanning Calorimetry. The Triton X-100 thermal properties were determined by differential scanning calorimetry (DSC) using a DSC 131 model Setaram calorimeter. Samples of 20 mg were weighed in 100 μL aluminum pans (6 mm base diameter, 4.2 mm deep). An empty pan was used as reference. An indium sample was used as calibration standard for both temperature and heat flow (mp 429.7 K, heat of melting 3263.5 J mol^{-1}). Measurements were carried out under a nitrogen atmosphere with a flow rate of around 20 mL min^{-1}.

The samples were submitted to a first heating for 5 min at 373 K to eliminate the water residues.

The influence of cooling rate on the thermal properties of Triton X-100 was evaluated carrying out different cooling/heating cycles between 373 and 143 K with cooling rates of 13 K min^{-1} (cycle I), 9 K min^{-1} (cycle II), 5 K min^{-1} (cycle III), 1 K min^{-1} (cycle IV), and 0.5 K min^{-1} (cycle V); the subsequent heating scans were carried out from 143 to 373 K always at a heating rate of 10 K min^{-1}.

The reversibility of the thermal transitions was verified by reheating the cooled sample just after the preceding scan up to its transition temperature.

The resolution of the heat flow was $\pm$0.2 μW. The melting temperatures (T_m) were obtained at the peak of the melting endothermic transition, and in a similar way the crystallization temperature (T_{cr}) either for cold- or for melt-crystallization was obtained at the peak of the respective exothermic transition. The glass transition temperatures (T_g) were taken at the inflection point (or midpoint) of the specific heat capacity increment in the transition. The enthalpies of fusion (ΔH_m) and the enthalpies of crystallization (ΔH_{cr}) were obtained from the areas under the curve that represents the overall calorimetric enthalpy of the process.

2.3. Polarized Optical Microscopy. Polarized optical microscopy was performed on an Olympus Bx51 optical microscope equipped with a Linkam LTS360 liquid nitrogen-cooled cryostage. The microstructure of the sample was monitored by taking microphotographs at appropriate temperatures and intervals of time, using an Olympus C5060 wide zoom camera. Images were obtained at a magnification of 500×. A drop of the sample (Triton X-100 and EGDMA) was squeezed between two microscope slides and inserted in the hot stage. The thickness of each squeezed sample was ca. 50 μm. Before each measurement, the Triton X-100 sample was heated to 373 K and kept 5 min at this temperature to allow complete melting. The same temperature history as followed by DSC was applied to observe the emergence of crystallinity under nonisothermal conditions by POM; to monitor isothermal cold- and melt-crystallization, the temperature treatment was the one followed by DRS. For EGDMA, the sample was kept 10 min at 313 K (T_m = 271.2 K) and cooled at 15 K min^{-1} to T_{cr} to follow melt-crystallization. For cold-crystallization, the sample was cooled from 313 at 15 K min^{-1} to 173 K and heated at the same rate to T_{cr}. Always a sporadic growth of spherulites was observed for EGDMA.

2.4. Dielectric Relaxation Spectroscopy. Dielectric measurements were carried out using the ALPHA-N impedance analyzer from Novocontrol Technologies GmbH. A drop of triton X-100 was placed between two gold plated electrodes (diameter 10 mm) of a parallel plate capacitor, BDS 1200, with two silica spacers, 50 μm thickness. The sample cell was mounted on a cryostat, BDS 1100, and exposed to a heated gas stream being evaporated from a liquid nitrogen Dewar. The temperature control is assured by the Quatro Cryosystem and performed within $\pm$0.5 K. Novocontrol Technologies GmbH supplied all of these modules. Before all dielectric measurements, the Triton X-100 sample was previously heated to 373 K, under the nitrogen stream, to eliminate residual water.

To study the thermal transitions of Triton X-100, isochronal measurements of the complex permittivity were carried out at 10^2 Hz, 10^3 Hz, 10^4 Hz, 10^5 Hz, and 1 MHz, during cooling/heating cycles with different cooling rates, and the subsequent heating was performed always at 9 K min^{-1}. The actual cooling

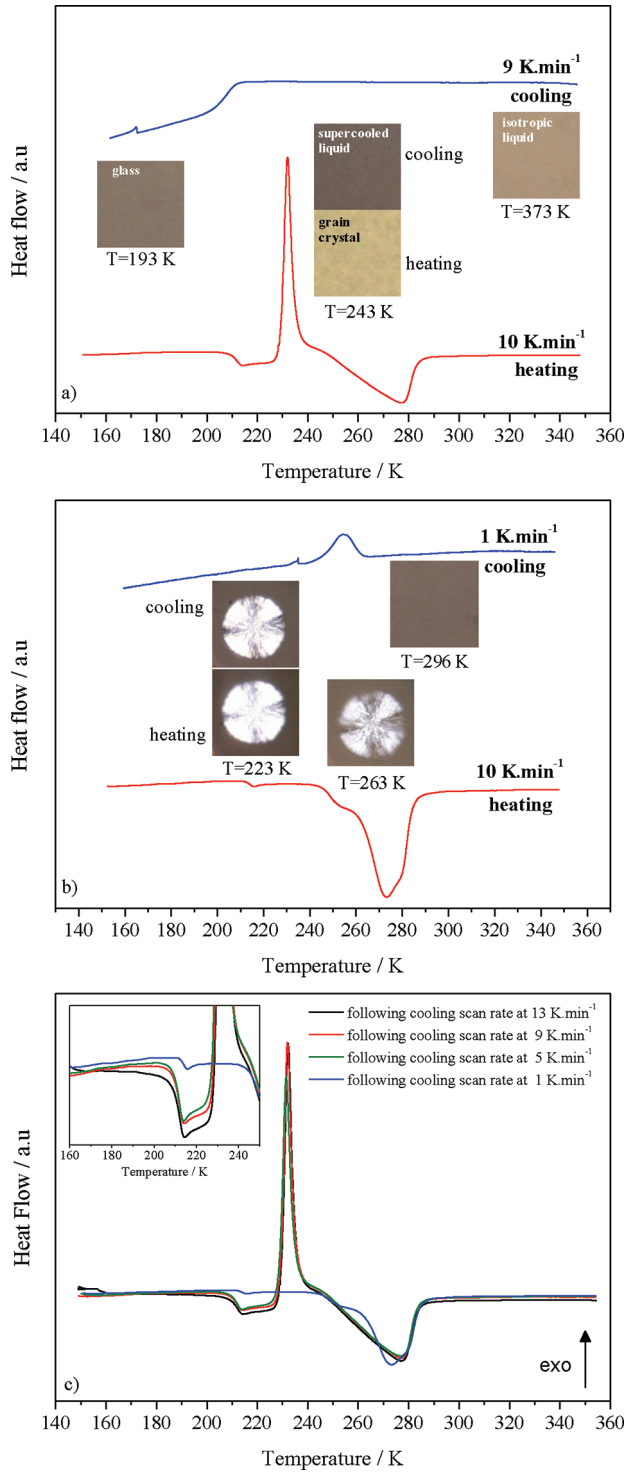

Figure 1. Thermograms (heat flow in arbitrary units, au, vs temperature) of Triton X-100 after water removal at 373 K collected at two cooling rates, (a) 9 K min^{-1} and (b) 1 K min^{-1}, and subsequent heating scans at 10 K min^{-1} as measured by differential scanning calorimetry; different heat flow scales were used for heating and cooling. (c) Heating scans collected at 10 K min^{-1} after all tested cooling rates; the inset is a scale-up of the glass transition region evidencing that the heat flux jump occurs in all heating scans. Microphotographs taken by POM at the specified temperatures on cooling from the liquid state at 10 K min^{-1} and on heating from the glass at 5 K min^{-1} are included in (a) and (b).

rates were 11 K min^{-1} (cycle 1), 7 K min^{-1} (cycle 2), 4 K min^{-1} (cycle 3), 1 K min^{-1} (cycle 4), and 0.5 K min^{-1} (cycle 5).

To monitor isothermal cold-crystallization, the sample was previously cooled from 373 to 173 K at 11 K min^{-1}. The sample then was rapidly heated to the cold-crystallization temperature, T_{cr} (219, 220, and 221 K), to avoid crystalline growth. Melt-crystallization was also studied at the same temperatures, T_{cr}, by performing real-time measurements in a sample directly cooled at 11 K min^{-1} from 373 K to the crystallization temperature.

At each T_{cr}, both cold- and melt-crystallizations were monitored by measuring the complex permittivity during successive frequency sweeps from 1 Hz to 1 MHz every 180 s over at least 5000 s.

Data Analysis. To analyze the isothermal dielectric data, the model function introduced by Havriliak−Negami[29] was fitted to both imaginary and real components of complex permittivity. Because multiple peaks are observed in the available frequency window, a sum of HN-functions is employed:

$$\varepsilon^*(f) = \varepsilon_0 + \sum_j \frac{\Delta\varepsilon_j}{[1 + (i\omega\tau_{HN})^{\alpha_{HN}}]^{\beta_{HN}}} \quad (1)$$

where j is the index over which the relaxation processes are summed, $\Delta\varepsilon$ is the dielectric strength, τ_{HN} is the characteristic HN relaxation time, and α_{HN} and β_{HN} are fractional parameters ($0 < \alpha_{HN} \leq 1$ and $0 < \alpha_{HN}\cdot\beta_{HN} \leq 1$) describing, respectively, the symmetric and asymmetric broadening of the complex dielectric function.[30] Conductivity effects were taken into account at the beginning of crystallization by adding a contribution $((\sigma_{DC})/(\varepsilon_0\omega))$ to the imaginary part of the fit function where σ_{DC} is the d.c. conductivity of the sample and ε_0 is the dielectric permittivity of vacuum.

From the estimated values of τ_{HN}, α_{HN}, and β_{HN} fitting parameters, a model-independent relaxation time, $\tau_{max} = 1/(2\pi f_{max})$, was determined according to the following equation:[30−32]

$$\tau_{max} = \tau_{HN} \times \left[\sin\left(\frac{\alpha_{HN}\pi}{2 + 2\beta_{HN}}\right)\right]^{-1/\alpha_{HN}} \left[\sin\left(\frac{\alpha_{HN}\beta_{HN}\pi}{2 + 2\beta_{HN}}\right)\right]^{-1/\alpha_{HN}} \quad (2)$$

3. RESULTS AND DISCUSSION

3.1. Differential Scanning Calorimetry. The thermal behavior of Triton X-100 was investigated in the temperature range between 143 and 373 K. It was observed that it crystallizes or vitrifies upon cooling from the equilibrium liquid depending on the cooling rate.

Figure 1 presents the DSC thermograms collected on cooling at two representative rates, (a) 9 K min^{-1} and (b) 1 K min^{-1}, and the subsequent heating run recorded at 10 K min^{-1}. For the thermogram collected at the highest cooling rate, no transition occurs down to ~210 K, the temperature at which the heat flux presents a discontinuity characteristic of the glass transition; the same is true for the thermogram collected on cooling at 13 K min^{-1} (not shown). Therefore, at these highest rates, it was possible to circumvent crystallization allowing one to obtain Triton X-100 as a supercooled liquid that becomes a glass upon further cooling, and so it is classified as a glass former.

Microphotographs taken by POM on cooling from 373 to 193 K at 10 K min^{-1} show an isotropic structure in the liquid state that remains in the supercooled region and glassy state (see Figure 1a, cooling).

Table 1. Thermal Properties of Triton X-100 Obtained by DSC during Different Cooling/Heating Cycles[a]

		cooling scan			heating scan at 10 K min^{-1}				
		glass transition	melt-crystallization		glass transition	cold-crystallization		melting	
cycle	rate (K min^{-1})	T_g/K	T_{cr}/K	ΔH_{cr}/J g^{-1}	T_g/K	T_{cr}/K	ΔH_{cr}/J g^{-1}	T_m/K	ΔH_m/J g^{-1}
I	13	206.7	n.o.	n.o.	212.2	232.2	−65.6	277.2	62.5
II	9	206.5	n.o.	n.o.	211.9	232.1	−64.8	277.2	61.6
III	5	208.0	227.3 248.5	−1.4 −0.8	212.0	231.5	−60.7	277.2	61.4
IV	1	n.o.[b]	254.7	−71.9	214.1	n.o.	n.o.	273.2	72.0
V	0.5	n.o.[b]	260.3	−81.4	data not available				

[a] T_g, glass transition temperature determined at the inflection point; T_m, melting temperature corresponding to the endothermic peak of the melting transition; T_{cr}, crystallization temperature corresponding to the exothermic peak of the crystallization transition; ΔH_m and ΔH_{cr}, melting and crystallization enthalpies, respectively. [b] It is not possible to give an accurate value.

By the other side, the thermogram collected at 1 K min^{-1} shows an exothermal peak centered at around 255 K (see Table 1). This is due to spherulitic crystallization confirmed by POM (see microphotograph in Figure 1b, cooling).

Melt-crystallization is also observed during cooling at 5 and 0.5 K min^{-1} (not shown), with a temperature onset that increases as the cooling rate decreases.

Concerning the subsequent heating runs presented in Figure 1a, for the one collected after cooling at 9 K min^{-1}, the heat flow jump reappears as the glass transition signature at a temperature of 212 K taken at the midpoint of the transition region (data provided in Table 1); this value of the glass transition temperature agrees with the values provided for Triton X-100 by Jensen et al.[33] (214.5 K measured at the midpoint) and by Larraz et al.[34] (205.15 K measured at the onset).

At higher temperatures, at 232 K, a sharp exothermic peak characteristic of cold crystallization emerges followed by a broad endothermic peak with minimum at 277 K, due to melting; details on temperatures and enthalpies are provided in Table 1. Cold-crystallization in the sample previously cooled at 10 K min^{-1} was also observed by POM by the appearance of a grain-like structure (microphotograph in Figure 1a, heating). This crystalline structure slowly melts, finally disappearing at around 273 K in accordance with the broad melting endotherm observed by DSC.

With the exception of the heating run taken after cooling at 1 K min^{-1}, all of the runs present the sharp exotherm due to cold-crystallization and posterior endotherm due to melting (Figure 1c). In fact, in the heating run measured after cooling at 1 K min^{-1}, no crystallization is observed, the main thermal event being an endotherm centered at 273 K corresponding to the melting of the crystalline fraction previously formed. The microphotograph taken by POM (Figure 1b, heating) evidences the partial melting of the spherulite that exhibits a weaker intense birefringence pattern as compared to the original one; once again, the melting occurs gradually as observed also by DSC. The absolute values of the enthalpies determined by DSC of previous crystallization and subsequent melting on heating are equal (72 J g^{-1}), confirming that the material in this condition did not undergo further cold crystallization. Moreover, the detection of the glass transition (scale-up in the inset of Figure 1c) reveals that the material, although crystallizing to a great extent as denoted by the high value of the crystallization enthalpy as compared to the other runs, is in the semicrystalline state. The glass transition step was detected in all cases, as evidenced in the inset, revealing that indeed in all runs a semicrystalline material was obtained.

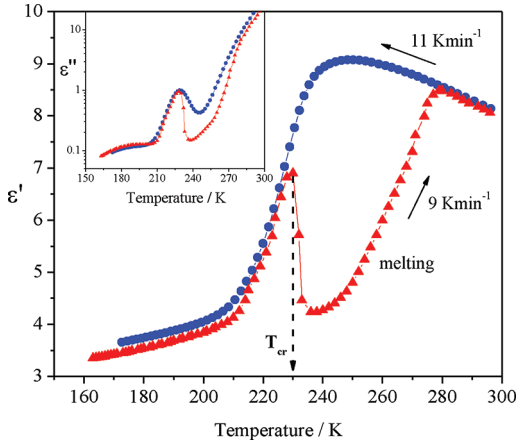

Figure 2. Isochronal plots of the real, ε', and imaginary, ε'' (inset), parts of the complex permittivity at 10 kHz collected in a cooling ramp from 298 to 160 K (gray ●) and the subsequent heating ramp (▲) carried at the specified rates; while crystallization was circumvented during cooling, the drop in both ε' and ε'' traces reveals that it occurred upon heating.

3.2. Dielectric Relaxation Spectroscopy. *3.2.1. Thermal Transitions Probed in Isochronal Mode.* The influence of cooling rate was also evaluated by DRS. Figure 2 presents the isochronal plots of both ε' and ε'' (in inset) at 10 kHz collected in the descending run to 160 K at the highest cooling rate (11 K min^{-1}). The corresponding heating run performed at 9 K min^{-1} is represented by black symbols.

The trace of the real part, ε', of the complex permittivity after an initial rise with the temperature decrease shows a marked fall indicating the transformation, at the measuring frequency, from the supercooled liquid to the glass; in the ε'' trace, this corresponds to an intense peak, that is, the α-relaxation process associated with the dynamical glass transition. At the lowest temperatures, a broad and low intense peak is observed due to a secondary relaxation. The detailed dielectric study of the different relaxation processes as a function of temperature will be reported elsewhere.

To confirm that no crystallization occurred during cooling, the increase observed in ε' trace will be taken now for analysis. This rise in the dielectric permittivity is related to the expected

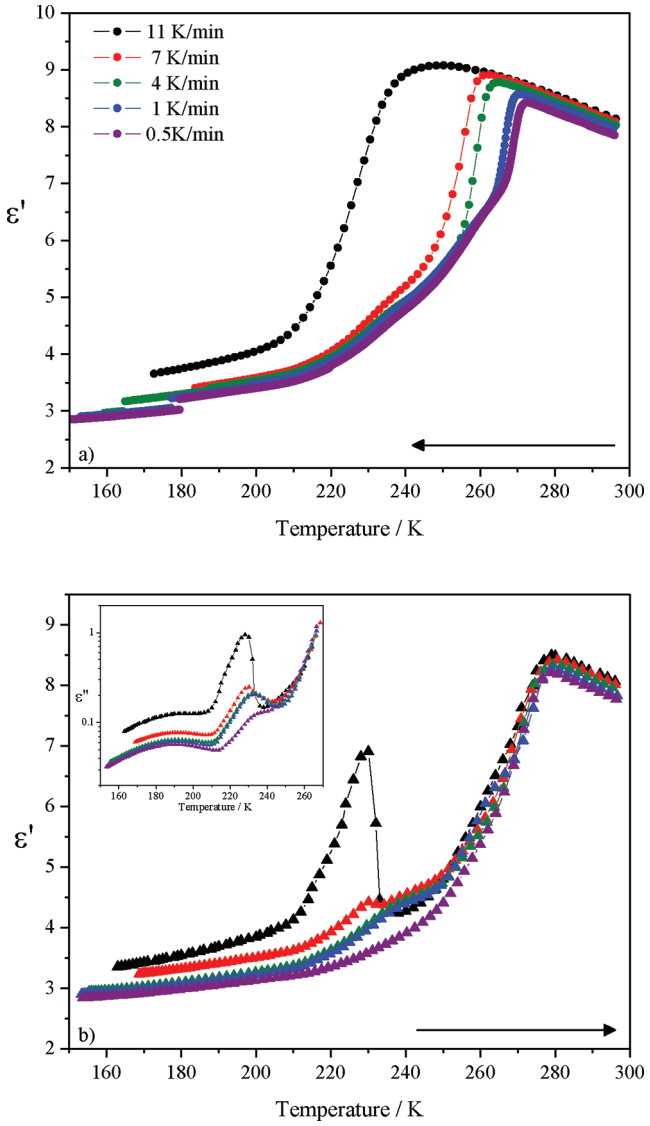

Figure 3. Isochronal plots of the real permittivity, ε', at 10 kHz during (a) cooling ramp experiments carried at different rates (see legend) and (b) the heating run, followed immediately after the cooling, which was performed always at the same rate (9 K min^{-1}) (same colors apply). The inset presents the corresponding isochronal loss trace, ε'', obtained during heating, evidencing the depletion in the α-process due to crystallization.

increase of the dielectric strength, which can be quantified according to the Fröhlich−Kirkwood equation:[30,35]

$$\varepsilon_s - \varepsilon_\infty = \frac{\mu_0^2 g^N / V \varepsilon_s (\varepsilon_\infty + 2)^2}{3\varepsilon_0 k_B T 3(2\varepsilon_s + \varepsilon_\infty)} \quad (3)$$

where μ_0 is the dipolar moment of the isolated dipole, g takes into account the dipole−dipole correlation (for parallel or antiparallel correlations between neighboring dipoles, $g > 1$ or $0 < g < 1$, respectively, while for a random orientation distribution of dipoles, $g = 1$), ε_s and ε_∞ are the limits of the real part of the dielectric permittivity at low and high frequencies, respectively, the latter being approximately the permittivity of the glass,[36] ε_0 is the vacuum permittivity, N/V is the number of dipoles per unit of volume, and k_B is the Boltzmann constant. Thus, from eq 3, the dielectric strength ($\Delta\varepsilon = \varepsilon_s - \varepsilon_\infty$) is proportional to $\mu_0^2 g/9\varepsilon_0 k_B T$. If it is assumed that g is constant, an increase in $\Delta\varepsilon$ from 375.4 to 249.6 K of 33.5% is predicted. The observed rise is 34.9% ($\varepsilon'_{375.4K}$ = 6.73; $\varepsilon'_{249.6K}$ = 9.08), confirming that no dipolar moment is lost due to immobilization that would occur if crystallization had taken place. Therefore, the absence of discontinuity in both ε' and ε'' traces upon cooling at 11 K min^{-1} until the region where the α-relaxation evolves led us to conclude that Triton X-100 crystallization was circumvented, reinforcing the DSC results.

Upon the subsequent heating, the fully amorphous sample undergoes cold-crystallization,[37,38] which is visible in the plot just above 230 K by an abrupt decrease in both ε' and ε''. The further increase in both real and imaginary parts observed near above 240 K is due to the progressive melting of the crystalline fraction thus formed; the ε' and ε'' values superimpose those of the equilibrium liquid at a temperature around 280 K, which is a frequency-independent thermal event. Both temperatures are in very good agreement with the onset and midpoint of the melting endothermic peak detected in the correspondent DSC heating thermogram, respectively, 243 K ($T_{m,on}$) and 277 K ($T_{m,peak}$).

Figure 3 shows the isochronal plots of ε' traces collected upon (a) cooling at different rates and (b) subsequent heating at 9 K min^{-1}.

The ε' trace obtained at a cooling rate of 11 K min^{-1} (Figure 3 a) acts as a reference for a run in which the sample does not undergo crystallization from the melt. Therefore, it was concluded that the sample undergoes crystallization in all runs except the one taken at the highest cooling rate. Moreover, the temperature at which crystallization occurs increases with the decrease of cooling rate. These observations are coherent with the previous reported DSC results.

In the following heating run, cold-crystallization is observed, as was already mentioned from the drop in the ε' trace when the sample was previously cooled at 11 K min^{-1} and by the decrease in the ε'' peak as well as shown in the inset (Figure 3b). In general, the ε'' peak associated with the dynamic glass transition observed on the heating run emerges smaller with the decrease of the cooling rate of the preceding run. A more detailed analysis reveals that in the heating run after cycle 3 no further cold-crystallization occurs: no drop in either the ε' or the ε'' trace is observed. This could lead us to conclude that the sample is fully crystalline. However, it stills in the semicrystalline state because a relaxational contribution associated with the glass transition exists (see the respective ε'' peak in the inset in Figure 3b), although it is significantly depleted.

For all runs, the endset of the melting is detected at the same temperature, close to 280 K, as observed in DSC.

Ramp experiments carried out at different cooling rates by either DSC or DRS proved that the glass-former Triton-X can be obtained with different extents of crystallinity, the slower rates promoting a higher crystallization, as expected.

DRS measurements evidence that a fully amorphous material is obtained when cooling from the liquid state at cooling rates higher than 10 K min^{-1}. On the other hand, a fully crystalline material could not be obtained by slow cooling experiments neither by DRS nor DSC.

3.2.2. Isothermal Crystallization. To get a further insight in the crystallization behavior, isothermal crystallization from both glassy and molten states was promoted and monitored in real time by dielectric relaxation spectroscopy at 219, 220, and 221 K (see Experimental Section). These temperatures were chosen because they allow simultaneously the detection of the α-process

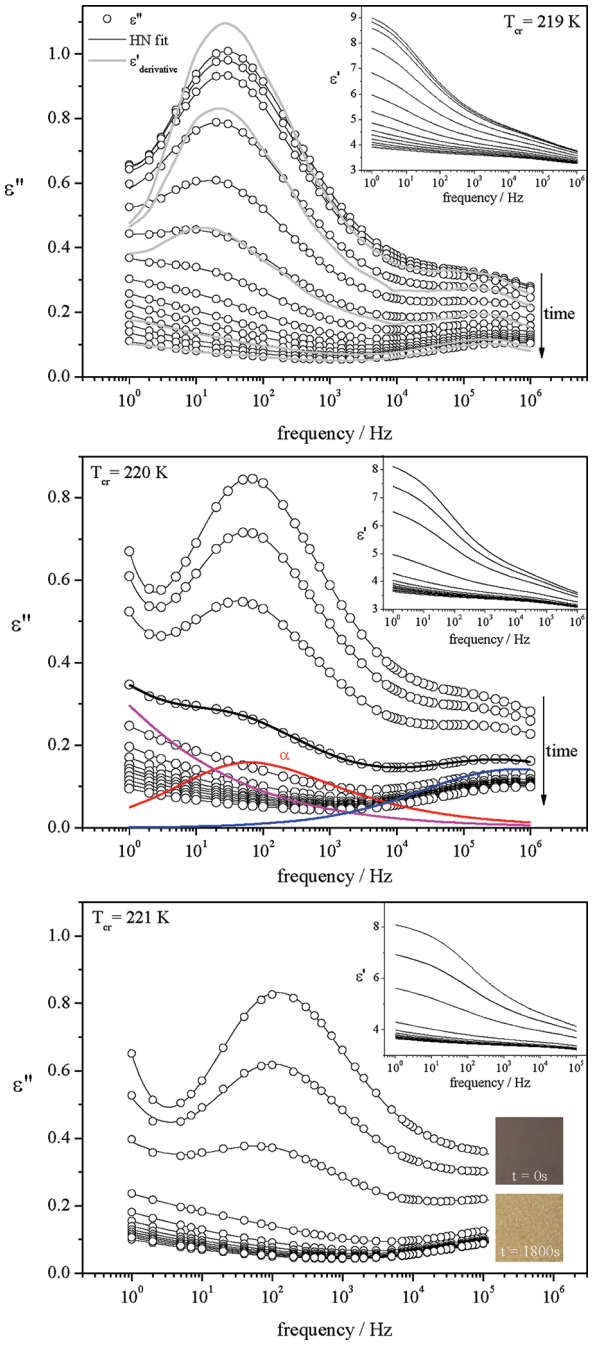

Figure 4. Real-time evolution of the imaginary part of the complex permittivity, $\varepsilon''(f)$, during isothermal cold-crystallization: only some representative loss spectra are illustrated, the two first spectra being 180 s apart and the following being 360 s apart. The α-process dominates the spectra, and the secondary relaxation influences the spectra in the high frequency side, while a low frequency process is needed to adequately simulate the loss data. Solid lines are the overall fit where a sum of 3 HN individual processes was considered (see text); these 3 HN processes are exemplified for T_{cr} = 220 K for the spectrum taken at 720 s (thicker solid line). For T_{cr} = 219 K, the logarithmic derivative of the real permittivity is represented for some crystallization times as gray thicker solid lines, allowing one to eliminate the conductivity contribution from ε''. For T_{cr} = 221 K, POM microphotographs taken at the initial time and after 1800 s were included; a scale-up of the grainy morphology observed at t_{cr} = 1800 s is shown later in Figure 7. The inset represents the evolution of the respective real part $\varepsilon'(f)$.

within the experimental frequency window and the amorphous−crystalline interconversion in a reasonable time. Figure 4 shows the collected loss spectra for cold-crystallization at some representative times. It must be noted that the same profile was obtained during real-time measurements for melt-crystallization at the same temperature, at each T_{cr}, that being the reason it is not shown here. The main observation is the strong depletion of the α-process. At the high frequency flank of the dominant process, the secondary relaxation is detected; an additional process is also felt at the lowest frequencies. Whether this process is a MWS one or an α'-process as found in crystallizable systems of either polymeric[14,39−43] or low molecular weight materials,[22,26,27,44] or even the simultaneous contribution of a secondary process, which is merged under the main alpha process in the fully amorphous material or a low frequency one, it is not clear up to now. This process should not be confused with conductivity, because the latter only affects the spectra at the first crystallization times. This is demonstrated by carrying out the analysis proposed by Wübbenhorst and van Turnhout,[45] an alternative to the numerical Kramers−Kronig transform, based on the logarithmic derivative of the real permittivity given by $\varepsilon''_{der} = -\pi/2(\partial\varepsilon'(\omega)/\partial \ln \omega)$ that allows one to eliminate the conductivity contribution from ε''. In Figure 4 for T_{cr} = 219 K, ε''_{der} is plotted at some definite crystallization times (thicker solid lines) where the coincidence between the experimental and the estimated ε'' for longer crystallization times is obvious, reinforcing that the low frequency contribution is other than conductivity. Therefore, a sum of three processes was considered in the HN fit to the experimental ε' and ε'' data (eq 1). The parameters of the individual functions used to fit the complex permittivity spectra for each temperature and type of crystallization are summarized in Table 2; because the peak of the low frequency process never shows up at any of the tested crystallization temperatures, no fitting parameters will be provided here. It was found that for all tested crystallization temperatures, both real and imaginary parts of the complex permittivity spectra are perfectly fitted by maintaining fixed both α_{HN} and β_{HN} shape parameters and τ_{HN} of the main process; the overall fit to ε'' is presented in Figure 4 as solid lines. Therefore, the α-relaxation keeps both shape and location invariants during isothermal crystallization (either cold or melt). The secondary relaxation also keeps the same shape; the respective relaxation times were allowed to vary, but no significant shift was observed (see limits in Table 2).

From the HN fit, the dielectric strength, $\Delta\varepsilon$, is also obtained (see eq 1). Its time evolution during both cold- and melt-crystallization for each T_{cr} is shown in Figure 5.

The variation with the crystallization time of the dielectric strength reduced by the initial value can be used to estimate the crystallinity degree (χ_{cr}), considering that the relaxation intensity is proportional to the amount of noncrystalline phase.[36] When crystallization leads to the extinction of the main α-process and no significant dielectric response persists in the detected processes observed in the frequency window that is being probed, it is common to consider χ_{cr} as $1 - (\Delta\varepsilon_{\alpha,t}/\Delta\varepsilon_{\alpha,0})$.[25−27] However, it is clear from both Figures 4 and 5 that the secondary process is still active after the vanishing of the α-relaxation. Therefore, the simultaneous contribution of both processes will be taken into account to quantify the degree of crystallinity according to:

$$\chi_{cr}(t) = 1 - \frac{\Delta\varepsilon_\alpha(t) + \Delta\varepsilon_\beta(t)}{\Delta\varepsilon_\alpha(t=0) + \Delta\varepsilon_\beta(t=0)} \quad (4)$$

The time dependence of the crystallinity degree thus estimated at each T_{cr} for cold- and melt-crystallization is plotted in Figure 5

Table 2. HN Parameters (α_{HN}, β_{HN}, τ_{HN}) Fixed in the Fitting Procedure to the Complex Permittivity Spectra during Isothermal Cold- and Melt-Crystallization[a]

			α-relaxation			secondary relaxation		
	T_{cr}/K	α_{HN}	β_{HN}	τ_{HN}/s	τ_{max}/s	α_{HN}	β_{HN}	τ_{HN}/s[b]
cold-crystallization	219	0.58	0.57	1.35×10^{-2}	5.49×10^{-3}	0.50	0.36	t_{0s} 2.5×10^{-6} → t_{8640s} 1.3×10^{-6}
	220	0.58	0.57	6.25×10^{-3}	2.51×10^{-3}	0.49	0.36	t_{0s} 1.7×10^{-6} → t_{7560s} 1.2×10^{-6}
	221	0.59	0.57	3.09×10^{-3}	1.28×10^{-3}	0.56	0.36	t_{0s} 1.6×10^{-6} → t_{4500s} 1.1×10^{-6}
melt-crystallization	219	0.60	0.57	1.34×10^{-2}	5.64×10^{-3}	0.45	0.36	t_{0s} 2.9×10^{-6} → t_{8640s} 1.4×10^{-6}
	220	0.55 ± 0.04	0.56	$(6 \pm 0.4) \times 10^{-3}$	$(2.4 \pm 0.2) \times 10^{-3}$	0.42	0.36	t_{0s} 1.8×10^{-6} → t_{7560s} 1.4×10^{-6}
	221	0.58	0.57	3.5×10^{-3}	1.42×10^{-3}	0.51	0.36	t_{0s} 2.7×10^{-6} → t_{4500s} 1.6×10^{-6}

[a] τ_{max} is the model-independent relaxation time obtained from τ_{HN} (eq 2). [b] The τ_{HN} values varied between the given limits during crystallization.

(red ●), never attaining unity, which means that the final material is not fully crystalline. Nevertheless, a highly crystalline material was obtained at the end of each isothermal crystallization coming from either glassy or molten states as evaluated by the depletion of the dielectric strength of the remaining processes that is much less than 1% of the original magnitude of the main α-relaxation.

Isothermal crystallization was also monitored by POM at some definite temperatures including 221 K. In Figure 4c, the microphotographs taken at the beginning of crystallization (100% amorphous sample) and after 30 min were included, the latter clearly showing that the sample is crystalline at the extent of the microscope resolution presenting a uniform grain like morphology.

The fact that the α-relaxation depletes with no changes in the relaxation time can be taken as an indication that the domain size of the cooperative motion underlying the dynamic glass transition is sufficiently small relative to the distance between crystallites, so the growing crystal units do not perturb dipole relaxation.[25,46] This behavior was observed also for other nonpolymeric materials such as ethylenoglycol dimethacrylate,[27] isooctyloxycyanobiphenyl,[20] and pharmaceutical drugs.[24,25] The detection of the secondary process after the vanishing of the cooperative α-relaxation suggests that the molecular motions that are in its origin occur in dimensions below the length scale of cooperativity.

A common treatment in literature to analyze the transformation from the disordered amorphous into the ordered crystalline phase at a fixed temperature is the Avrami model.[28,47,48] In this treatment of the isothermal crystallization kinetics, different nucleation and growth mechanisms have correspondingly different time dependences of the crystallization rate that can be modeled by the Avrami law,[28] which can be described in terms of the normalized real permittivity, ε'_N. Therefore, to extract kinetic information of Triton X-100, the real permittivity at 500 Hz, a frequency for which the low frequency process does not influence the α-process so strongly, was taken and normalized:[20,36,49]

$$\varepsilon'_N(t) = \frac{\varepsilon'(0) - \varepsilon'(t)}{\varepsilon'(0) - \varepsilon'(\infty)} \quad (5)$$

where $\varepsilon'(0)$ is the dielectric permittivity at the start of the crystallization, $\varepsilon'(\infty)$ is the long time limiting value, and $\varepsilon'(t)$ is the value at the allowed time for crystallization, t. Figure 6 presents the semilogarithmic plot of ε'_N as a function of time at each crystallization temperature; no significant differences were found between the time evolution of the normalized values of both type of crystallizations. For the case of considering ε'_N, the Avrami law reads:

$$\varepsilon'_N(t) = 1 - \exp(-kt^n) \quad (6)$$

where k is a temperature-dependent rate constant, and n is the Avrami parameter that can take values between 1 and 7 depending on nucleation type and crystal growth mechanism.[20,50] A plot of $\ln[-\ln(1 - \varepsilon'_N(t))]$ versus $\ln t$ gives a straight line having n as the slope and $-\ln k$ as the intercept (linearization of eq 6). The corresponding plot is shown in the inset of Figure 6 for both types of crystallization. The linearization does not hold for the entire time range; nevertheless, for $T_{cr} = 219$ K, it was possible to analyze the linear behavior at the shortest crystallization times; the obtained n and k values for crystallization carried at 219 K are presented in Table 3. The almost flat region at longer times at each T_{cr} corresponds to an invariant crystallization degree achieved.

Alternatively, the kinetic analysis can be carried out by rewriting the Avrami equation taking into account t_0, the induction time preceding crystallization and a characteristic time for the isothermal crystallization, τ_{cr}:[28,51]

$$\varepsilon'_N(t) = 1 - \exp\left[-\left(\frac{t - t_0}{\tau_{cr}}\right)^n\right] \quad (7)$$

where $\varepsilon'_N(t)$ is the fraction transformed in the crystalline phase at time (t), and τ_{cr} is obtainable from the Avrami parameters by the relationship $\tau_{cr} = k^{-1/n}$. Equation 7 is the basis of a modified method of data analysis proposed by Avramov et al.,[51] which is more sensitive to the changes in the time scale of τ_{cr}, avoiding problems due to a noncorrect evaluation of t_0 or lack of thermal stability in collecting the first experimental points.[49]

Figure 6 shows the normalized values of the real permittivity for cold- and melt-crystallizations carried out at the three temperatures. To estimate τ_{cr}, t_0, and n, eq 7 was directly fitted to $\varepsilon'_N(t)$ data corresponding to the solid lines in the figure; the semilogarithmic plot enhances the agreement obtained for the shortest times being especially sensitive to the value of the induction time. The estimated quantities are included in Table 3.

The n values found are below 2, which, in light of the model, could be interpreted as a crystal growth of low dimensionality.

Concerning the τ, k, and n kinetic parameters here estimated for Triton X-100, it is interesting to compare them to those found for ethylene glycol dimethacrylate, EGDMA, which also carries an ethylene oxide unity. While isothermal crystallization for EGDMA was monitored in the temperature range $0.87 \leq T_g/T_{cr} \leq 0.92$,[27] for Triton X-100, the crystallization was followed between $0.95 \leq T_g/T_{cr} \leq 0.96$, much closer to the glass

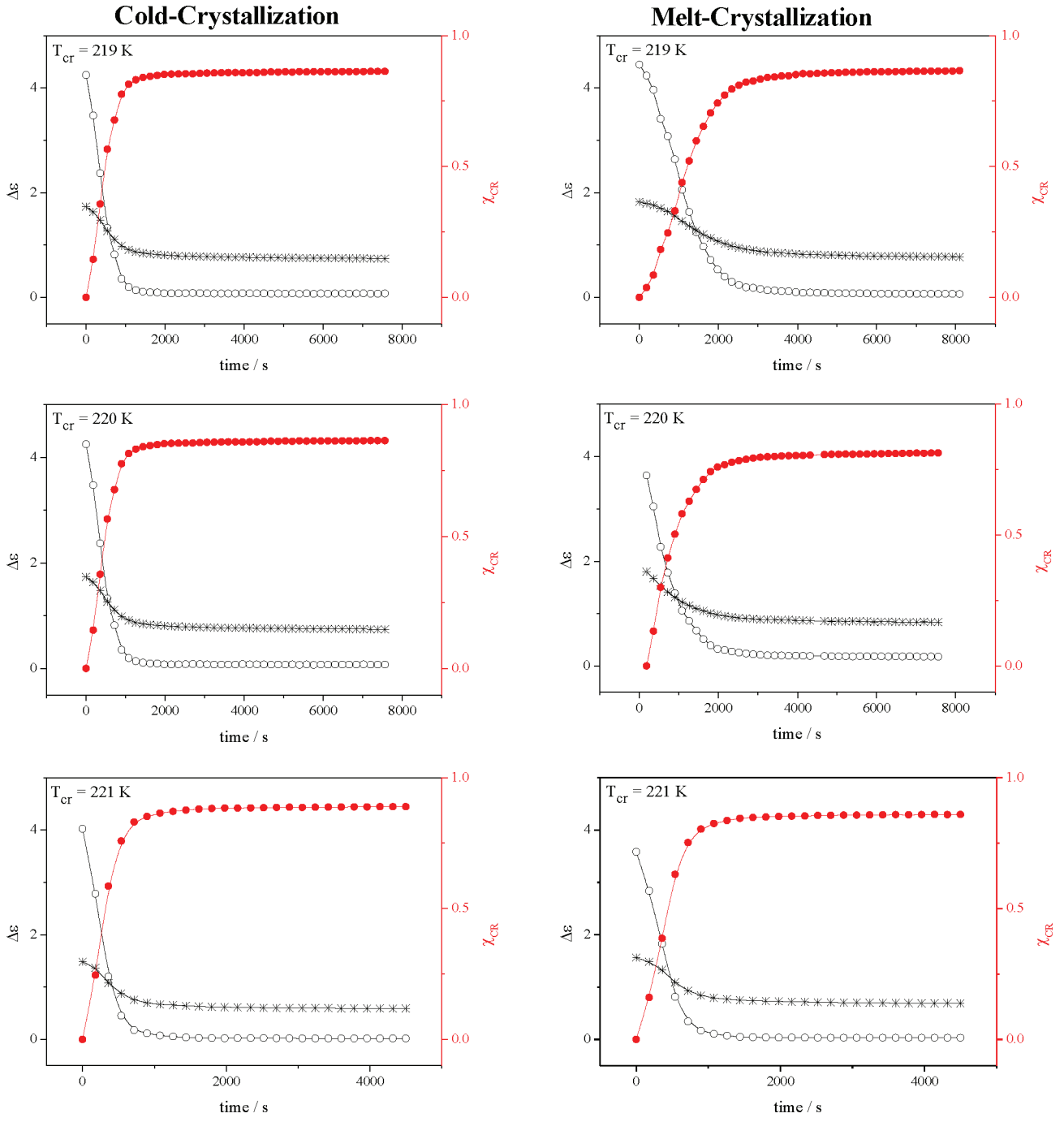

Figure 5. Real-time evolution of the dielectric strength, $\Delta\varepsilon$, obtained from the fit of a sum of three HN functions to the complex permittivity spectra collected during cold- (left plots) and melt-crystallization (right plots) at the indicated crystallization temperatures, T_{cr} = 219, 220, and 221 K; "○" correspond to the α-relaxation and "*" to the secondary-process (both in the left axis). In the right axis, time dependence of the crystallinity degree, χ_{cr} (red ●), is reported. Lines are guides for the eyes.

transition temperature. In particular, the τ and k kinetic parameters here estimated for Triton X-100 at 219 K, only 6 K above T_g, are in close agreement with those found for ethylene glycol dimethacrylate, EGDMA ($\tau_{cr,EGDMA}$ = 1459 ± 56 s; k_{EGDMA} = 8.66×10^{-6} $s^{-1.6}$)[52] for isothermal cold-crystallization carried at 193 K, that is, 17 K above T_g. Moreover, for the lowest temperature at which isothermal crystallization of EGDMA was monitored (187 K), 11 K above T_g, with $\log(\tau_{max})$ of the α-relaxation close to −3, almost no crystallization was observed, while the crystallization of Triton X-100 was carried out at 221 K (9 K above T_g), having almost the same $\log(\tau_{max})$, as it crystallizes at a high rate and to a great extent over comparable scales of time.

To rationalize this behavior, it is important to understand how crystallization evolves. This phenomenon is usually interpreted[53] in terms of a nucleation/growth process, meaning that the occurrence of crystallization requires the presence of nuclei (nanosize clusters) on which the crystals will subsequently

dx.doi.org/10.1021/jp2028033 |J. Phys. Chem. B 2011, 115, 12336–12347

growth (micrometer-size crystals).[54] For a variety of materials, the nucleation rate has a maximum above T_g, while the maximum growth rate is further displaced at higher temperatures somewhere between T_g and T_m.[2,55,56] The rate of nucleation and growth of the clusters of the newly evolving crystalline phase is dictated by the rate of the diffusion of the ions/molecules that build the crystalline phase.[54] Therefore, to allow diffusion to occur, it seems reasonable to assume that some segmental motion enabled by the α-process is required, as was observed previously for EGDMA.[27,44]

To compare the segmental mobility between the two compounds, a T_g scaled plot of the respective relaxation times, τ_{max}, corresponding to the α-process detected at each T_{cr}, was drawn in Figure 7; the relaxation times of EGDMA were obtained from the τ_{HN} values taken from Table 1 of reference 27 by using eq 2.

It is evident the higher steepness of the mobility of Triton X-100 with the temperature, revealing a higher fragility index, m, relative to EGDMA. The fragility index is a quantitative measure of the degree of deviation from Arrhenius-type temperature dependence near T_g, providing a useful classification of glass formers in terms of fragility. Materials are called "strong" if they show a $\tau(T)$ dependence close to an Arrhenius-type behavior and "fragile" if their $\tau(T)$ significantly deviates from linearity, induced by high cooperative molecular rearrangements.[57] The fragility index, m, is defined as the derivative:

$$m = -\left(\frac{\mathrm{d}\log\tau(T)}{\mathrm{d}(T_g/T)}\right)_{T=T_g} \quad (8)$$

Fragility values typically range between $m = 16$ for strong systems and $m = 200$ for fragile ones.

A high dynamic fragility is interpreted as a high cooperativity between relaxing units, that is, a high coupling of the dynamics of a specific relaxing unity with its environment. It was proposed by Sanz et al.[58] that this can have a positive impact on the probability of occurrence of nuclei pointing to a correlation between nucleation kinetics and dynamic fragility when crystallization occurs near the glass transition, with higher fragility implying a higher nucleation rate.

However, Mijóvic and Sy[15] suggested that a higher nucleation rate could be the origin of a grain-like morphology exhibited by PLA upon cold-crystallization.

Applying these ideas to the systems here studied, we predict that Triton X-100 by exhibiting higher dynamic fragility should have a higher nucleation rate and therefore a crystalline morphology closer to grain-like when crystallization occurs near T_g. Indeed, this morphology was already observed for the temperatures at which isothermal crystallization was carried out (remember Figure 4 for T_{cr} = 221 K). To answer this question in more detail, isothermal crystallization at different temperatures was also monitored by POM for Triton X-100 and EGDMA (see Experimental Section). For Triton X-100, in the tested T_{cr} range ($T_m - T \approx 57$ K), a grain-like microstructure with no optically resolvable spherulites is always observed, while sporadic growth of three-dimensional spherulites was observed for EGDMA in either melt- or cold-crystallization (see microphotographs in Figure 7). Moreover, for Triton X-100, it was found that the crystalline morphology depends on the degree of undercooling ($T_m - T$), with it being observed that shperulites emerge when crystallization is promoted at temperatures between 233 and 253 K (24 K $\leq T_m - T \leq$ 44 K); representative POM images are included in Figure 7. A similar dependence of morphology with the degree of undercooling is also reported for PLA[15] and for a semicrystalline polyimide.[59] For the latter, it is claimed that the nucleation density increases sharply with small increases in the degree of undercooling, with a concomitant decrease in the spherulitic size, the fine grainy morphology being attributed to a catastrophic nucleation density.[59]

The correlation between dynamic fragility and the ability of Triton X-100 to crystallize in the proximity of the glass transition could also be analyzed under another perspective: the higher fragility index of Triton X-100 means that for small temperature

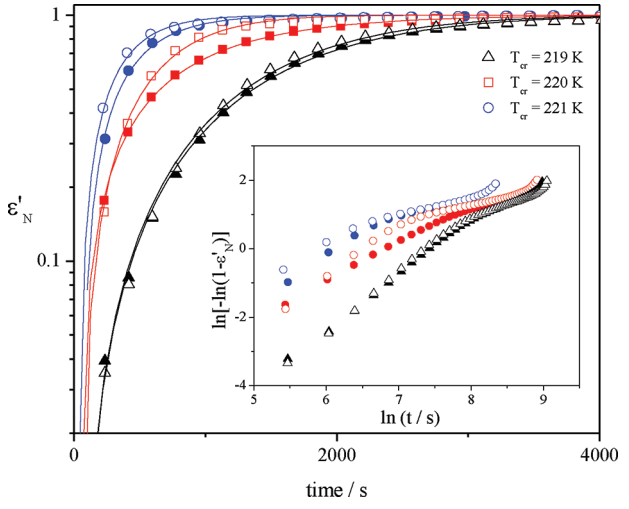

Figure 6. Semilogarithmic plot of the time evolution of the normalized real permittivity, ε'_N, for both cold- (open symbols) and melt-crystallization (filled symbols), evidencing how well eq 7 describes data from the initial times; the inset shows the double logarithmic Avrami plot of ε'_N.

Table 3. Kinetic Parameters Obtained from the Fit of Equation 7 to the Normalized Real Permittivity for Both Melt- and Cold-Crystallizations at Each T_{cr}[a]

		cold-crystallization				melt-crystallization			
	temperature/K	t_o/s	τ_{cr}/s	k/s^{-n}	n	t_o/s	τ_{cr}/s	k/s^{-n}	n
Avrami equation (eq 7)	221	34 ± 10	334 ± 14	$(1.5 \pm 0.5) \times 10^{-3}$	1.12 ± 0.05	58 ± 16	405 ± 18	$(1.2 \pm 0.3) \times 10^{-3}$	1.12 ± 0.4
	220	43 ± 17	646 ± 22	$(1.7 \pm 0.5) \times 10^{-4}$	1.34 ± 0.04	40 ± 7	874 ± 10	$(8 \pm 2) \times 10^{-4}$	1.05 ± 0.03
	219	34 ± 27	1596 ± 32	$(7 \pm 2) \times 10^{-6}$	1.61 ± 0.03	39 ± 23	1675 ± 28	$(9 \pm 2) \times 10^{-6}$	1.57 ± 0.03
double ln Avrami plot	219	–[b]	$(1.6 \pm 0.4) \times 10^3$	$(1.9 \pm 0.3) \times 10^{-6}$	1.78 ± 0.02	–[b]	$(1.8 \pm 0.4) \times 10^3$	$(3.5 \pm 0.6) \times 10^{-6}$	1.68 ± 0.02

[a] In the last row, kinetic parameters obtained from the Avrami linearization (double logarithmic plot of $\varepsilon'_N(t)$) taken at the shortest times of both crystallizations carried at 219 K. [b] The t_0 value cannot be directly determined from the double logarithmic linearization.

dx.doi.org/10.1021/jp2028033 |J. Phys. Chem. B 2011, 115, 12336–12347

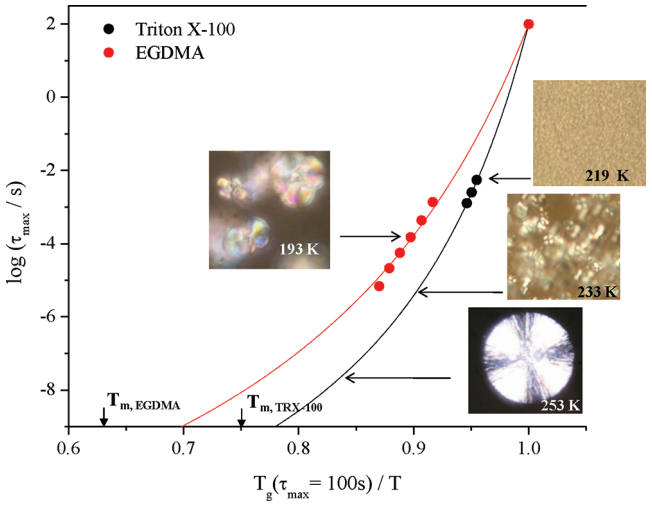

Figure 7. T_g scaled plot of the temperature dependence of relaxation times of the α-process for Triton X-100 and EGDMA; the slope of the plot at T_g is a measure of the fragility index, m, corresponding to the derivative $(\partial \log(\tau(T))/\partial(T_g/T))_{T=Tg}$ (see text), being higher for Triton X-100. The solid lines were calculated according to the equation proposed by Böhmer et al.[60]

changes near T_g, coming from the glassy state, its relaxation time decreases more deeply relative to the less fragile EGDMA, and thus Triton X-100 becomes more mobile closer to T_g. This could promote the segmental motion that enables its crystallization to a greater extent than EGDMA at the same T_g/T_{cr}. However, this is not the only factor that determines the way how crystallization evolves. As mentioned earlier, if we compare crystallization in the two compounds at the same τ_{max} ($\sim 10^{-3}$ s), Triton X-100 (221 K) undergoes a rapid crystallization and to a great extent ($\chi_{cr,\ TritonX\text{-}100} > 90\%$, in the first 25 min), while EGDMA (187 K) almost does not crystallize ($\chi_{cr,EGDMA} \approx 10\%$ after 2 h 30 min).

Note that $\log \tau = \log \tau_{Tg} - 16 + 256 \times (T_g)/(T)/(m - (m - 16) \times (T_g)/T)$, with $m_{TritonX\text{-}100} = 125$ and $m_{EGDMA} = 81$. Microphotographs obtained by POM taken at the indicated temperatures are included, evidencing how the crystalline morphology of Triton X-100 varies with the undercooling degree ($T_m - T_{cr}$); a POM microphotograph representative of the spherulite morphology of EGDMA is also included.

The analysis of the mobility by one side and of the morphology by the other side seems to suggest that the molecular motions involved in the formation of the crystalline structure in the proximity of the glass transition in Triton X-100 are of smaller length scale relative to those governing crystallization in EGDMA, which is an interesting result. In fact, the mobility needed to a molecule to be incorporated in the neighboring crystallite in a grain-like morphology is of lower dimensionality than those that lead to a three-dimensional spherulite, with the latter observed for EGDMA. This is compatible with the lower values of the estimated Avrami exponents for Triton X-100 ($1.12 \leq n \leq 1.6$) as compared to those for EGDMA ($1.6 \leq n \leq 3$)[27] by DRS. We must note that it is usual to obtain lower n values from dielectric data for several glass former systems,[19,20,36,61] even when the observed morphology is compatible with higher n values predicted by the Avrami theory.[36] It was claimed that this can be due an inadequacy of the model to describe crystallization in complex processes where it occurs concomitantly with the formation of a rigid amorphous fraction (observed for EGDMA and conceivable for Triton X-100).[19] If this is a failure of the model in these complex processes or a true different nucleation/growth mechanism induced by a different experimental setup of DRS relative to POM or DSC, it is not clear up to now. The simultaneous utilization of all of these different techniques, as done by Wurm et al.,[62] providing information on the molecular mobility and on the emerging morphology, to probe the same sample in the same holder under crystallization, would be advantageous to clarify this aspect.

In any case, the n Avrami exponents for EGDMA and Triton X-100 were estimated by following identical protocols, so there is no doubt that the latter has a lower n value.

This behavior of Triton X-100 can be a consequence of the particular dynamical behavior of surfactants that undergo self-association and chain packing of the hydrophobic chain imprinting some preorder that enables further crystallization. The high fragility index ($m \approx 125$) indicates a high intermolecular cooperative segmental dynamics, meaning that neighboring units relax in a highly coupled way. This could lead to locally structured domains like mesomorphic structures that act as an intermediate preordering step preluding the crystal formation as was suggested to occur in other materials.[63]

Finally, no difference in the kinetic behavior was found for Triton X-100 between cold- and melt-crystallization. In some materials either polymeric as PLLA[18] or nonpolymeric as EGDMA,[27] there is an acceleration of the cold-crystallization process relative to melt-crystallization due to the increment of the number of crystallization nuclei at the beginning of cold-crystallization, with a significant temperature shift between the formation of crystallization nuclei and further growing. In Triton X-100, the cooling below T_g before the induction of cold-crystallization did not accelerate the crystallization process relative to melt-crystallization, at least in the probed crystallization temperature range. This can indicate that no additional nuclei formation occurred during additional cooling, and therefore its formation and growing may occur almost simultaneously as rationalized for melt-crystallization.[27] This seems compatible with the occurrence of catastrophic nucleation/crystallization that gives rise to a grainy morphology as observed by POM at the tested T_{cr}, coming from either molten or glassy states, giving rise to the simultaneous crystallization of all of the sample as far as optical resolution allows one to observe.

4. CONCLUSIONS

Temperature-driven phase transformations undergone by the surfactant Triton X-100 were investigated by DSC and DRS and complemented by POM. It was observed that crystallization can be circumvented if the material is cooled at a rate ≥ 10 K min^{-1}. This means that under these specific conditions, it is possible to enlarge $\sim$60 K the temperature range where TritonX-100 exhibits liquid and supercooled liquid properties, with vitrification occurring only around 206 K; this ability could advantageously be used in different applications as cryopreservation of biological systems.

For cooling rates under 10 K min^{-1}, crystallization is always observed, emerging at temperatures that are higher the lower is the cooling rate. When the material is cooled at a rate ≥ 5 K min^{-1}, cold-crystallization is always observed upon subsequent heating.

It was observed by POM that the attained morphology upon crystallization depends on the undercooling degree.

In the proximity of the glass transition, for the highest undercooling degree ($T_m - T_{cr} \approx 57$ K), a grain-like morphology is detected, while large and more perfect spherulites emerge for lower undercooling degree ($24 \text{ K} \leq T_m - T_{cr} \leq 44$ K).

The evolution of the dielectric α-process and secondary relaxation were followed during cold- and melt-crystallization at $T_{cr} = 219$, 220, and 221 K, near the glass transition, with no significant changes in either the position or the shape. The secondary relaxation observed in the high frequency flank of the α-peak still persists even when the complete depletion of the α-relaxation was observed.

From the time evolution of the normalized real permittivity, kinetic parameters were extracted considering a modified Avrami law taking into account the induction time. The reason that isothermal crystallization occurs to a great extent in the vicinity of the glass transition was rationalized as the simultaneous effect of (i) a high dynamic fragile behavior and (ii) the occurrence of catastrophic nucleation/crystal growth probably enabled by a preordering tendency of the surfactant molecules.

The ability of Triton X-100 to undergo vitrification and crystallization coming from the molten state or from the glass makes it a model compound to investigate temperature-driven phase transformations.

AUTHOR INFORMATION

Corresponding Author

*E-mail: madalena.dionisio@dq.fct.unl.pt.

ACKNOWLEDGMENT

We acknowledge Professor J. L. Gómez Ribelles for fruitful discussions. This work was supported by Fundação para a Ciência e Tecnologia (FCT, Portugal) through projects PTDC/CTM/69145/2006, PTDC/CTM/64288/2006, and PTDC/CTM/098979/2008. M.T.V. acknowledges FCT for a postdoctoral grant SFRH/BPD/39691/2007.

REFERENCES

(1) Carpentier, L.; Decressain, R.; Desprez, S.; Descamps, M. *J. Phys. Chem. B* **2006**, *110*, 457–464.
(2) Andronis, V.; Zografi, G. *J. Non-Cryst. Solids* **2000**, *271*, 236–248.
(3) Vallet-Regí, M.; Granado, S.; Arcos, D.; Gordo, M.; Cabañas, M. V.; Ragel, C. V.; Salinas, A. J.; Doadrio, A. L.; San Román, J. *J. Biomed. Mater. Res.* **1998**, *39*, 423–428.
(4) Walstra, P. *Physical Chemistry of Food*; Marcel Dekker Inc.: New York, 2003; Chapter XVI.
(5) Hancock, B. C.; Shamblin, S. L.; Zografi, G. *Pharm. Res.* **1995**, *12*, 799–806.
(6) Yoshioka, M.; Hancock, B. C.; Zografi, G. *J. Pharm. Sci.* **1995**, *84*, 983–986.
(7) Dudognon, E.; Danède, F.; Descamps, M.; Correia, N. T. *Pharm. Res.* **2008**, *25*, 2853–2858.
(8) Bhugra, C.; Rambhatla, S.; Bakri, A.; Duddu, S. P.; Miller, D. P.; Pikal, M. J.; Lechuga-Ballesteros, D. *J. Pharm. Sci.* **2007**, *96*, 1258–1269.
(9) Seefeldt, K.; Miller, J.; Alvarez-Núñez, F.; Rodríguez-Hornedo, N. *J. Pharm. Sci.* **2007**, *96*, 1147–1158.
(10) Yuan, H. Z.; Cheng, G. Z.; Zhao, S.; Miao, X. J.; Yu, J. Y.; Shen, L. F.; Du, Y. R. *Langmuir* **2000**, *16*, 3030–3035.
(11) London, E.; Brown, D. A. *Biochim. Biophys. Acta* **2000**, *1508*, 182–195.
(12) Asami, K. *J. Phys.: Condens. Matter* **2007**, *19*, 376102.
(13) Williams, G. *Adv. Polym. Sci.* **1979**, *33*, 59–92.
(14) Ezquerra, T. A.; Baltá-Calleja, F. J.; Zachmann, H. G. *Polymer* **1994**, *35*, 2600–2606.
(15) Mijović, J.; Sy, J. W. *Macromolecules* **2002**, *35*, 6370–6376.
(16) Fitz, B. D.; Andjelić, S. *Polymer* **2003**, *44*, 3031–3036.
(17) Dionísio, M.; Viciosa, M. T.; Wang, Y.; Mano, J. F. *Macromol. Rapid Commun.* **2005**, *26*, 1423–1427.
(18) Brás, A. R.; Viciosa, M. T.; Wang, Y.; Dionísio, M.; Mano, J. F. *Macromolecules* **2006**, *39*, 6513–6520.
(19) Laredo, E.; Graimau, M.; Barriola, P.; Bello, A.; Müller, A. J. *Polymer* **2005**, *46*, 6532–6542.
(20) Massalska-Arodz, M.; Williams, G.; Thomas, D. K.; Jones, W. J.; Dabrowski, R. *J. Phys. Chem. B* **1999**, *103*, 4197–4205.
(21) Hédoux, A.; Denicourt, T.; Guinet, Y.; Carpentier, L.; Descamps, M. *Solid State Commun.* **2002**, *122*, 373–378.
(22) Minoguchi, A.; Nozaki, R. *J. Non-Cryst. Solids* **2002**, *307–310*, 246–251.
(23) Sanz, A.; Jiménez-Ruiz, M.; Nogales, A.; Martín y Marero, D.; Ezquerra, T. A. *Phys. Rev. Lett.* **2004**, *93*, 015503.
(24) Rengarajan, G. T.; Beiner, M. *Lett. Drug Des. Discovery* **2006**, *3*, 723–730.
(25) Alie, J.; Menegotto, J.; Cardon, P.; Duplaa, H.; Caron, A.; Lacabanne, C.; Bauer, M. *J. Pharm. Sci.* **2004**, *93*, 218–233.
(26) Dobbertin, J.; Hannemann, J.; Schick, C.; Potter, M.; Dehne, H. *J. Chem. Phys.* **1998**, *108*, 9062–9068.
(27) Viciosa, M. T.; Correia, N. T.; Salmerón Sanchez, M.; Carvalho, A. L.; Romão, M. J.; Gómez Ribelles, J. L.; Dionísio, M. *J. Phys. Chem. B* **2009**, *113*, 14209–14217.
(28) Avrami, M. *J. Chem. Phys.* **1939**, *7*, 1103–1112. **1940**, *8*, 212–224. **1941**, *9*, 177–184.
(29) Havriliak, S.; Negami, S. *Polymer* **1967**, *8*, 161–210. Havriliak, S.; Negami, S. *J. Polym. Sci., Part C: Polym. Symp.* **1966**, *14*, 99–117.
(30) Schönhals, A.; Kremer, F. Analysis of Dielectric Spectra. In *Broadband Dielectric Spectroscopy*; Kremer, F., Schönhals, A., Eds.; Springer Verlag: Berlin, 2003; Chapter 3.
(31) Boersema, A.; Van Turnhout, J.; Wübbenhorst, M. *Macromolecules* **1998**, *31*, 7453–7460.
(32) Schröter, K.; Unger, R.; Reissig, S.; Garwe, F.; Kahle, S.; Beiner, M.; Donth, E. *Macromolecules* **1998**, *31*, 8966–8972.
(33) Jensen, R. E.; O'Brien, E.; Wang, J.; Bryant, J.; Ward, T. C.; James, L. T.; Lewis, D. A. *J. Polym. Sci., Part B: Polym. Phys.* **1998**, *36*, 2781–2792.
(34) Larraz, E.; Elvira, C.; San Román, J. *J. Polym. Sci., Part A: Polym. Chem.* **2003**, *41*, 1641–1649.
(35) Fröhlich, H. *Theory of Dielectrics*; Clarenton Press: Oxford, 1958.
(36) Massalska-Arodz, M.; Williams, G.; Smith, I. K.; Conolly, C.; Aldridge, G. A.; Dabrowski, R. *J. Chem. Soc., Faraday Trans.* **1998**, *94*, 387–394.
(37) Wunderlich, B. *J. Chem. Phys.* **1958**, *29*, 1395–1404.
(38) Diogo, H. P.; Moura Ramos, J. J. *J. Chem. Educ.* **2006**, *83*, 1389.
(39) Shafee, E. El. *Eur. Polym. J.* **2001**, *37*, 1677–1684.
(40) Fukao, K.; Miyamoto, Y. J. *J. Non-Cryst. Solids* **1997**, *212*, 208–214. Fukao, K.; Miyamoto, Y. J. *J. Non-Cryst. Solids* **1998**, *235−237*, 534–538.
(41) Mierzwa, M.; Floudas, G. *IEEE Trans. Dielectr. Electr. Insul.* **2001**, *8*, 359–364 (reproduced in Floudas, G. Effect of Pressure on the Dielectric Spectra of Polymeric Systems. In *Broadband Dielectric Spectroscopy*; Kremer, F., Schonhals, A., Eds.; Springer Verlag: Berlin, 2003; Chapter 8).
(42) Cerveny, S.; Zinck, P.; Terrier, M.; Arrese-Igor, S.; Alegría, A.; Colmenero, J. *Macromolecules* **2008**, *41*, 8669–8676.
(43) Alves, N. M.; Mano, J. F.; Balaguer, E.; Meseguer Dueñas, J. M.; Gómez Ribelles, J. L. *Polymer* **2002**, *43*, 4111–4122.
(44) Viciosa, M. T.; Correia, N. T.; Salmerón Sanchez, M.; Gómez Ribelles, J. L.; Dionísio, M. *J. Phys. Chem. B* **2009**, *113*, 14196–14208.
(45) Wübbenhorst, M.; van Turnhout, J. *J. Non-Cryst. Solids* **2002**, *305*, 40–49.
(46) Andjelic, S.; Fitz, B. D. *J. Polym. Sci., Part B: Polym. Phys.* **2000**, *38*, 2436–2448.
(47) Doremus, R. H. *Rates of Phase Transformations*; Academic Press: Orlando, FL, 1985.

(48) Gutzow, I.; Schmelzer, J. *The Vitreous State: Thermodynamics, Structure, Rheology, and Crystallization*; Springer-Verlag: Berlin, 1995.
(49) Napolitano, S.; Wübbenhorst, M. *J. Non-Cryst. Solids* **2007**, *353*, 4357–4361.
(50) Meares, P. *Polymers, Structure and Bulk Properties*; Van Nostrand: London, 1965. Cowie, J. M. G. *Polymers, Chemistry and Physics of Modern Materials*; Blackie: Glasgow, 1991 (quoted in ref 20).
(51) Avramov, I.; Avramova, K.; Rüssel, C. *J. Cryst. Growth* **2005**, *285*, 394–399.
(52) The value of *k* is incorrect in ref 27; the correct value is the one here provided.
(53) Shelby, J. E. *Introduction to Glass Science and Applications*; Royal Society of Chemistry: Cambridge, UK, 2002.
(54) Fokin, V. M.; Schmelzer, J. W. P.; Nascimento, M. L. F.; Zanotto, E. D. *J. Chem. Phys.* **2007**, *126*, 234507.
(55) Rao, C. N. R.; Rao, K. J. *Phase Transitions in Solids*; McGraw-Hill: New York, 1978.
(56) Owen, A. E. *Amorphous Solids and the Liquid State*; Plenum: New York, 1985.
(57) Böhmer, R.; Angell, C. A. *Phys. Rev. B* **1992**, *45*, 10091–10094.
(58) Sanz, A.; Nogales, A.; Ezquerra, T. A. *Macromolecules* **2010**, *43*, 29–32.
(59) Ratta, V.; Ayambem, A.; Youn, R.; McGrath, J. E.; Wilkes, G. L. *Polymer* **2000**, *41*, 8121–8138.
(60) Böhmer, R.; Ngai, K. L.; Angell, C. A.; Plazek, D. J. *J. Chem. Phys.* **1993**, *99*, 4201–4209.
(61) Mansour, A. A.; Saad, G. R.; Hamed, A. H. *Polymer* **1999**, *40*, 5377–5391.
(62) Wurm, A.; Minakov, A. A.; Schick, C. *Eur. Polym. J.* **2009**, *45*, 3282–3291.
(63) Lund, R.; Alegría, A.; Goitandía, L.; Colmenero, J.; González, M. A.; Lindner, P. *Macromolecules* **2008**, *41*, 1364–1376.